Hydrol. Earth Syst. Sci. Discuss., 11, 12697–12729, 2014
www.hydrol-earth-syst-sci-discuss.net/11/12697/2014/
doi:10.5194/hessd-11-12697-2014


Hydrology and Earth System Sciences
Open Access
Discussions



# Understanding NMR relaxometry of partially water-saturated rocks

**O. Mohnke, C. Nordlund, R. Jorand, and N. Klitzsch**

Institute for Applied Geophysics and Geothermal Energy (GGE), E.ON Energy Research Center (E.ON ERC), RWTH Aachen University, Mathieustrasse 10, 52074 Aachen, Germany

Received: 16 September 2014 – Accepted: 20 September 2014
– Published: 17 November 2014

Correspondence to: O. Mohnke (omohnke@eonerc.rwth-aachen.de)

Published by Copernicus Publications on behalf of the European Geosciences Union.







## Abstract

Nuclear Magnetic Resonance (NMR) relaxometry measurements are commonly used to characterize the storage and transport properties of water-saturated rocks. These assessments are based on the proportionality of NMR signal amplitude and relaxation time to porosity (water content) and pore size, respectively. The relationship between pore size and NMR relaxation time depends on pore shape, which is usually assumed to be spherical or cylindrical. However, the NMR response at partial water saturation for natural sediments and rocks differs strongly from the response calculated for spherical or cylindrical pores, because these pore shapes cannot account for water menisci remaining in the corners of de-saturated angular pores. Therefore, we consider a bundle of pores with triangular cross-sections. We introduce analytical solutions of the NMR equations at partial saturation of these pores, which account for water menisci of de-saturated pores. After developing equations that describe the water distribution inside the pores, we calculate the NMR response at partial saturation for imbibition and drainage based on the deduced water distributions.

For this pore model, NMR amplitude and NMR relaxation time at partial water saturation strongly depend on pore shape even so the NMR relaxation time at full saturation only depends on the surface to volume ratio of the pore. The pore-shape-dependence at partial saturation arises from the pore shape and capillary pressure dependent water distribution in pores with triangular cross-sections. Moreover, we show the qualitative agreement of the saturation dependent relaxation time distributions of our model with those observed for rocks and soils.

## 1 Introduction

Understanding multi-phase flow processes in porous rocks and soils is vital for addressing a number of problems in the geosciences such as oil and gas recovery or vadose zone processes, which influence groundwater recharge and evaporation.





HESSD
11, 12697–12729, 2014



Effective permeability, which is defined as the permeability of a fluid in presence of another fluid, is the decisive parameter for fluid transport, and depends on fluid saturation, wetting condition, and pore structure. In addition, saturation history influences the fluid content and the effective permeability (for a specific pressure), which are different for imbibition and drainage.

A method considered suitable for determining water content of rocks non-invasively is nuclear magnetic resonance (NMR), because the NMR signal amplitudes are directly proportional to the hydrogen content in the pore space, and the NMR relaxation times are linked to the size of the water-containing pores in the rock. In a two-phase system of water and air only the water contributes to the NMR signal response. Therefore, NMR is widely used for estimating transport and storage properties of rocks and sediments (Kenyon, 1997; Seevers, 1966; Fleury et al., 2001; Arnold et al., 2006).

In recent years, several researchers have studied the relationship between NMR and multiphase flow behavior on the pore scale to better understand and infer the storage and transport properties of partially saturated rocks or sediments (e.g., Chen et al., 1994; Liaw et al., 1996; Ioannidis et al., 2006; Jia et al., 2007; Al-Mahrooqi et al., 2006; Costabel and Yaramanci, 2011, 2013; Talabi et al., 2009). As an extension of this research, we study the relationship between the water distribution inside the pores of a partially saturated rock and the system's NMR response by using bundles of pore with triangular cross-sections. While Al-Mahrooqi et al. used a similar modeling approach to infer the wettability properties in oil-water systems, this study investigates the evolution of the NMR relaxation-time spectra during drainage and imbibition. For this purpose, we consider a capillary pore ensemble that is partially saturated with water and air. Traditionally, the pores within this ensemble are assumed to have a cylindrical geometry. Depending on pressure, cylindrical capillaries are either water- or air-filled and thus they either contribute to an NMR response or they do not. Consequently, the NMR relaxation times of partially water-saturated capillary pore bundles always remain subsets of the fully saturated system's relaxation-time distribution, i.e., they are a function inside the envelope of the distribution curve at full saturation (see Fig. 1a).





HESSD
11, 12697–12729, 2014



However, in porous rocks, which are formed by the aggregation of grains, the pore geometry is usually more complex (Lenormand et al., 1983; Ransohoff and Radke, 1987; Dong and Chatzis, 1995) and may exhibit angular and slit-shaped pore cross-sections rather than cylindrical capillaries or spheres (Fig. 2a). For example, in tight gas reservoir rocks Desbois et al. (2011) found three types of pore shapes that are controlled by the organization of clay sheet aggregates: (i) elongated or slit-shaped, (ii) triangular, and (iii) multi-angular cross-sections. The relaxation-time distribution functions derived from NMR measurements for such partially saturated rocks are frequently found to be shifted towards shorter relaxation times outside the original envelope observed for a fully saturated sample, (Fig. 2b) (e.g., Applied Reservoir Technology Ltd., 1996; Stingaciu, 2010; Stingaciu et al., 2010).

In angular pores, water will remain trapped inside the pore corners even if the gas entry pressure is exceeded. Standard NMR pore models that assume cylindrical or spherical pore-ensembles (e.g., Kenyon, 1997), however, do not account for such residual water (Blunt et al., 2002; Finjord et al., 2006; Tuller et al., 1999; Or and Tuller, 2000; Tuller and Or, 2001). To overcome this limitation, we introduce numerical simulations and analytical solutions of the NMR equations for partially saturated pores with triangular cross-sections to quantify NMR signal amplitudes and relaxation times. The NMR response of a triangular capillary during drainage and imbibition depends on the water distribution inside the capillary, which is subject to pore shape and capillary pressure. Thus, in the next chapter we present the relationship between capillary pressure andwater distribution inside cylindrical and triangular pore geometries during drainage and imbibition. For this purpose, the reduced similar geometry concept introduced by Mason and Marrow (1991) is used. Subsequently, based on the spatial water distribution, an analytical solution of the NMR diffusion equation (Torrey, 1956; Brownstein and Tarr, 1979) for partially saturated triangular capillaries is derived and tested by numerical simulations (Mohnke and Klitzsch, 2010). The derived equations are used to study the influence of pore size distribution and pore shape of triangular capillaries on the NMR response, in particular considering the effects of trapped water. Finally, an





HESSD
11, 12697–12729, 2014



approach for simulating NMR signals during imbibition and drainage of triangular pore capillaries is introduced and the simulated signals are tested using synthetic pore size distributions.

## 2 Results and discussion

### 2.1 Water distribution during drainage and imbibition in a partially saturated triangular tube

In a partially saturated pore space, a curved liquid–vapor interface called the arc meniscus (AM) arises due to the pore's capillary forces. In addition, adsorptive forces between water and matrix lead to the formation of a thin water film at the rock–air interface. Such water films with a thickness typically below 20 nm (e.g., Toledo et al., 1990; Tokunaga and Wan, 1997) exhibit very short NMR relaxation times. Although water films to some extent may influence transport properties and water distribution of a partially saturated porous system (Tuller and Or, 2001), the contribution of the film volume to NMR amplitudes is very small with respect to the NMR signal amplitudes arising from the water trapped in the menisci, i.e., $V_{\text{film}} \ll V_{\text{meniscus}}$. Therefore, for sake of simplicity, we neglect water films in his study.

In the following discussion, we consider a triangular capillary, initially filled with a perfectly wetting liquid, i.e., contact angle $\theta = 0^{\circ}$, which exhibits a constant interfacial tension $\sigma$ ($\sigma_{\text{air–water}} = 73 \times 10^{-3}\,\text{Nm}^{-1}$ at 20 °C) and is under the assumption that gravity forces are weak. The two-phase capillary entry pressure as derived by the MS-P method (Mayer and Stowe, 1965; Princen, 1969a, b, 1970) can be expressed by the Young–Laplace equation:

$$p_{\text{c}} = \frac{\sigma \cos\theta}{r_{\text{AM}}} = \frac{\sigma}{r_{\text{AM}}}, \tag{1}$$

where $r_{\text{AM}}$ is the radius of the interface arc meniscus and $p_{\text{c}}$ is the minimum pressure difference necessary for a non-wetting fluid, i.e., air, to invade a uniformly wetted





HESSD
11, 12697–12729, 2014



(tri-)angular tube filled with a denser phase, i.e., water (see Fig. 3a). Upon consideration of a pressure difference $p > p_c$, the non-wetting fluid will begin to enter the pore and occupy the central portion of the triangle, whereas – separated by the three interface arc menisci of radius $r_{AM}$ – the wetting fluid remains in the pore corners (Fig. 3a).

From an original triangle $ABC$, a new smaller triangle $A'B'C'$ of similar geometry with an inscribed circle of radius $r' = r_{AM} < R_0$ can be constructed by means of the reduced similar geometry concept as introduced by Mason and Morrow (1991) (Fig. 3b). To account for different transport mechanisms during imbibition and drainage of the denser wetting phase, Mason and Morrow (1991) introduced two different principal displacement curvatures with radii $r_I$ and $r_D$, respectively.

During imbibition of a (tri-)angular pore, the radius of curvature $r_{AM}$ increases until the separate arc menisci of the corners touch and the pore fills spontaneously ("snap off"). The critical radius of curvature $r_I$, which is equal to the radius of the pore's inscribing circle, for the angular pore at "snap-off" pressure $p_I$ is then given by

$$r_I = \frac{2A}{P}, \tag{2}$$

According to Eq. (2), the snap-off pressure depends on the geometry of the triangle only, i.e., on its cross-sectional area $A$ and perimeter $P$. In contrast, during drainage the threshold radius of curvature $r_D = r_{AM}$, at which the center of the fully saturated angular capillary spontaneously empties as a non-wetting fluid phase invades the pore, is given by

$$r_D = P\left[\frac{1}{2G} + \left(\frac{\pi}{G}\right)^{1/2}\right]^{-1}, \tag{3}$$

with $r_D < r_I$ and drainage threshold pressure $p_D > p_I$. The dimensionless and size-independent factor $G = \frac{A}{P^2}\left(= \frac{A'}{P'^2}\right)$ reflects the shape of the triangle depending on its cross-sectional area $A$ and perimeter $P$ ($A'$ and $P'$ refer to the reduced triangle), i.e.,





HESSD
11, 12697–12729, 2014



from near-slit-shape ($\lim_{\gamma \to 0} G = 0$) to equilateral shape ($G = 0.048$). A detailed derivation of Eqs. (2) and (3) as a consequence of hysteresis between drainage and imbibition can be found in Mason and Morrow (1991).

Combining Eqs. (1)–(3) with the concept of reduced similar geometry discussed above, the degree of water saturation ($S_w$) inside a single triangular tube with cross-sectional area $A_0$, perimeter $P_0$, and radius $R_0$ of its inscribing circle at a given capillary pressure $p_c$ during imbibition and drainage can be calculated according to

$$S_w^I(p, A_0, P_0) = \begin{cases} 1, & p_c \le p_I(R_0 \le r_I) \\ \frac{A_\Delta(p_c)}{A_0}, & p_c > p_I(R_0 > r_I) \end{cases} \quad \text{(imbibition)} \tag{4}$$

$$S_w^D(p_c, A_0, P_0) = \begin{cases} 1, & p_c < p_D(R_0 < r_D) \\ \frac{A_\Delta(p_c)}{A_0}, & p_c \ge p_D(R_0 \ge r_D) \end{cases} \quad \text{(drainage)} \tag{5}$$

The total area $A_\Delta$ of the triangular tube's water retaining corners, $\gamma_i, i = 1,2,3$, i.e., the gray areas in Figs. 4 and 5) is expressed by

$$A_\Delta(p_c) = \sum_{i=1}^{3} A_{\gamma_i}(p_c), \tag{6a}$$

where

$$A_{\gamma_i}(p_c) = \left( \frac{1}{\tan \frac{\gamma_i}{2}} - \frac{(\pi - \gamma_i)}{2} \right) r_{AM}^2(p_c), \quad 0 < \gamma_i < \pi \tag{6b}$$

is the area of the triangle's $i$th water-filled corner (Tuller and Or, 1999). Consequently, the total effective area $A_\Delta$ still occupied by water is equal to the difference between the (reduced) triangular pore area $\tilde{A}$ and the area $\pi r_{AM}^2$ of its respective inscribing circle (see Fig. 3). Eq. (6) a can be simplified to $A_\Delta = (3\sqrt{3} - \pi) r_{AM}(p_c)$ when considering equilateral triangles, i.e., $\gamma_i = \frac{\pi}{3}, i = 1,2,3$. The radius $r_{AM}(p_c)$ of the reduced triangle's





HESSD
11, 12697–12729, 2014



arc meniscus can be directly calculated from Eq. (1). Calculated pressure-dependent water and gas distributions during imbibition and drainage for an equilateral and arbitrary triangular capillary are shown in Figs. 4a and 5a. The corresponding water retention curves plotted in Figs. 4b and 5b illustrate the resulting hysteresis behavior of the partially saturated system and can be subdivided into three parts: at low capillary pressures, i.e., $p_c < p_I$, the pore always remains fully water-saturated. For the interval $p_I < p_c \leq p_D$, two separate behaviors are observed: during imbibition, the water content gradually increases with increasing capillary pressure, while during drainage the pore still remains fully saturated. For pressure levels $p_c \geq p_D$, both drainage as well as imbibition exhibit the same gradual decrease of water saturation.

In the following section, analytical solutions for respective NMR responses that arise from partially saturated arbitrary triangular tubes are derived and validated with numerical simulations of the NMR diffusion equations.

### 2.2 NMR response for triangular capillaries

NMR relaxometry is commonly employed for petrophysical investigations of saturated porous rocks in well-logging and laboratory studies. In this respect, the NMR method is a unique geophysical tool, which delivers direct information about the water content and allows to infer the pore-size distribution in rock samples or the subsurface. The measured NMR relaxation signal $M(t)$ is constituted by superposition of all signal-contributing pores in a rock sample (e.g., Coates et al., 1999; Dunn et al., 2002):

$$\frac{M(t)}{M_0} = \frac{1}{V_0} \sum_{i}^{N} \left( v_i \times (1 - e^{t \cdot T_{i,1}^{-1}}) \right), \tag{7}$$

where $M_0$ and $V_0$ are the equilibrium magnetization and total volume of the pore system, respectively. The saturated volume of the $i$th pore and its corresponding longitudinal relaxation constant are given by $v_i$ and $T_{i,1}$, respectively.





HESSD
11, 12697–12729, 2014



Following derivations of Brownstein and Tarr (1979), the inverse of the longitudinal relaxation time $T_1$ is linearly proportional to the surface-to-volume ratio of a pore according to

$$T_1^{-1} = T_{1B}^{-1} + \rho \frac{S_a}{V}, \tag{8}$$

where $T_{1B}$ is the bulk relaxation time of the free fluid and $\rho$ is the surface relaxivity, a measure of how quickly protons loose orientation or phase coherence due to magnetic interactions at the fluid–solid interface, which can be attributed to paramagnetic ions at mineral grain surfaces. $V$ and $S_a$ are the pore's volume and active surface boundaries, respectively. In this context, an active boundary refers to an interfacial area, i.e., the pore wall, where $\rho > 0$ and, thus, enhanced NMR relaxation will occur as the molecules diffuse to the wall. This model, however, is based on the general assumption of a relaxation regime that is dominated by surface relaxation processes, i.e., the fluid molecules move sufficiently fast and thus explore all parts of the pore volume with respect to the time scale ($\sim T_1$) of the experiment.

Upon consideration of a long (triangular) capillary, its surface-to-volume-ratio equals its perimeter-to-cross-section-ratio, i.e., $S/V = P/A$. Consequently, Eq. (8) can be written as

$$T_1^{-1} = T_{1B}^{-1} + \rho \frac{P_0}{A_0}, \tag{9}$$

where $P_0$ is the saturated tube's (active) perimeter and $A_0$ its cross-sectional area for a circular cross-section, $\frac{P_0}{A_0} = \frac{2}{r_0}$, with $r_0$ being the capillary radius. Hence, the relaxation rate of a fully saturated arbitrary triangular pore $ABC$ can be expressed in terms of its shape factor $G$ and perimeter $P_0$:

$$T_1^{-1} = T_{1B}^{-1} + \frac{\rho}{G P_0} \left( = T_{1B}^{-1} + \rho \frac{L_{AB} + L_{BC} + L_{CA}}{L_{AB} L_{CA} \sin(\gamma_A)} \right), \tag{10}$$





HESSD
11, 12697–12729, 2014



where $L_{AB}$, $L_{BC}$, and $L_{AC}$ are the lengths of a triangle's sides and $\gamma_A$ is the angle at corner $A$ (see Fig. 3). As illustrated in Fig. 6, the relaxation times decrease with decreasing pore shape factor $G$ and increasing pore perimeter $P$. By reducing one angle from 60 to 0° while fixing another at 60°, we increase $P/A$ for a constant cross-sectional area $A$. In the special case of an equilateral triangular capillary, i.e., $P_0/A_0 = \frac{12}{\sqrt{3}L_0}$, Eq. (10) can be simplified to

$$T_1^{-1} = T_{1B}^{-1} + \rho\frac{12}{\sqrt{3}L_0}. \tag{11}$$

Now we consider the previously discussed water–air system of a partially saturated equilateral triangular capillary. Here, the NMR signal will originate from the water retained at the corners. Replacing $A_0$ in Eq. (9) with an effective area $A_\gamma$ or $A_\Delta$ as derived by Eqs. (6a, b), respectively. $A_\Delta$ reflects the actual pore fraction that contributes to the NMR signal, i.e., the portion of the pore area $A_0$ that still remains occupied by water.

Supposing the air–water interface to be a passive boundary with respect to NMR surface relaxivity, i.e., $\rho = 0$, the effective active boundary is exclusively controlled by the pore wall segments ($\rho > 0$) in contact with water (wetting phase) (Fig. 7). Thus, the active perimeter of such a partially saturated triangular capillary is equal to its pressure-dependent reduced triangle's perimeter, $P'_\Delta\left(r^{I,D}(p_c)\right)$, according to

$$P_\Delta = \sum_{i=1}^{N=3} P_{\gamma_i}, \tag{12}$$

with

$$P_{\gamma_i} = 2\frac{r_{AM}(p_c)}{\tan\frac{\gamma_i}{2}}, \quad 0 < \gamma_i < \pi \tag{13}$$





HESSD
11, 12697–12729, 2014



being the perimeter of the $i$th water-filled corner. Consequently, the NMR relaxation rates and NMR signal (amplitude) evolution during drainage and imbibition of a single equilateral triangular capillary can be expressed by

$$T_{\Delta,1}^{-1} = \begin{cases} T_{1B}^{-1} + \rho \frac{P_0}{A_0}, & S_w^{I,D} = 1 \\ T_{1B}^{-1} + \rho \frac{P_\Delta^{I,D}(p_c, A_0, P_0)}{A_\Delta^{I,D}(p_c, A_0, P_0)}, & S_w^{I,D} < 1 \end{cases} \quad (14)$$

and

$$\frac{m(t)}{m_0} = S_w^{I,D}(p_c, A_0, P_0)\left(1 - e^{\frac{-t}{T_{\Delta,1}}}\right), \quad (15)$$

respectively. Illustrated in Fig. 8a is the pressure-dependent water distribution inside a single equilateral triangular capillary (with a side length of 1 µm) during drainage. The corresponding evolution of the longitudinal magnetization is shown in Fig. 8b. As the water saturation is reduced with increasing pressure, both NMR amplitudes and relaxation times (c) decrease. Note that only a single characteristic relaxation time at each saturation degree is observed, since each corner has the same $P_\gamma/A_\gamma$, and consequently the same $T_1$ value.

In contrast, each water-filled corner of a partially saturated non-equilateral triangle, i.e.,$\gamma_1 \neq \gamma_2 \neq \gamma_3$, can have a different $P_\gamma/A_\gamma$ ratio, and thus will show a different relaxation time and amplitude. As a result, depending on its individual shape, even a single partially saturated pore exhibits a multi-exponential NMR relaxation behavior based on Eq. (7) according to

$$\frac{m(t)}{m_0} = \frac{1}{A_0}\sum_{i=1}^{N=3} A_{\gamma_i}^{I,D}\left(1 - e^{\frac{-t}{T_{\gamma_i,1}}}\right), \quad (16)$$

with $T_{\gamma_i,1} = \frac{1}{T_{1B}} + \rho\frac{P_{\gamma_i}}{A_{\gamma_i}}$ and $\frac{A_{\gamma_i}^{I,D}}{A_0}$ being the characteristic relaxation time and amplitude contribution of the $i$th corner of the triangle, respectively. Figure 9 exemplifies such





HESSD
11, 12697–12729, 2014



different multi-exponential relaxation behavior for a pore with a right triangle geometry with angles of ($\gamma_1 = 30^\circ, \gamma_2 = 60^\circ, \gamma_3 = 90^\circ$) and the same cross-sectional area as the equilateral pores in Fig. 8 (i.e., ~ NMR porosity).

To test the analytical (fast diffusion) models for partially saturated triangular capillaries derived above, the calculated longitudinal NMR relaxation times and amplitudes are compared to solutions obtained from 2-D numerical simulations of the general NMR diffusion equation (Mohnke and Klitzsch, 2010):

$$\dot{m} = \left( D\nabla^2 - \frac{1}{T_B} \right) m, \tag{17}$$

with normalized initial values $m(r, t = 0) = \frac{M_0=1}{A}$ and boundary conditions

$$Dn\nabla m|_P = \rho_s m|_P, \tag{18}$$

where $m$ is the magnetization density, $D$ the diffusion coefficient of water, $T_B$ the bulk relaxation time, $\rho_s$ the interface's surface relaxivity, $n$ the outward normal, and $A$ and $P$ the pore's cross-sectional area and perimeter, respectively. The above equations were solved numerically using finite elements (Mohnke and Klitzsch, 2010) to simulate the respective NMR relaxation data of the studied triangular geometries.

As shown in Fig. 10, analytically (+ symbols in the figure) calculated NMR relaxation data for drainage and imbibition for an equilateral triangular pore are in a very good agreement ($R^2 > 0.99$) with data obtained from numerical simulations (o symbols in the figure).

The model was also validated for pores with arbitrary angles. Figure 11 illustrates 2-D numerical simulations using saturated pore corners with angles $\gamma_i$ ranging from 5 to 175° with equal active surface-to-volume ratios $P_{\gamma_i}/A_{\gamma_i}$ = const. and thus $T_{1,i}$ = const. The simulations were compared to their respective analytical solutions. The ratios of the numerical to the analytical model results for NMR amplitudes, i.e., NMR signal amplitudes, $A_\gamma$, and relaxation times, $T_{1,\gamma}$ as function of corner aperture $\gamma$ are shown





HESSD
11, 12697–12729, 2014



and confirm a near perfect correlation of $R^2 > 0.99$, with deviations generally less than 0.05 %. In this regard, the slight increase in divergence of relaxation time ratios at acute and obtuse angles can be attributed to numerical errors resulting from a decrease of the finite element's grid quality due to extremely high or low x-to-y ratios at these apertures (see Fig. 11a). Note that the above model is applicable to any angular capillary geometry such as square or octahedron.

### 2.3 Simulated water retention curves and NMR relaxation data of partially saturated pore distributions

The goal of this section is to evaluate how a forward-modeled NMR response of a system of pores is affected by pore shapes, i.e., triangular or circular pore capillaries. As discussed earlier, when a single capillary pore is fully water-saturated, its NMR relaxation time is inversely proportional to its perimeter-to-surface ratio. Thus, the relaxation-time distribution obtained from a multi-exponential NMR relaxation signal represents the pore-size distribution of the rock. In practice, the NMR pore-size distribution of a rock is calibrated by comparing the NMR relaxation-time distributions of a water-saturated rock with the pore throat size distribution obtained from mercury injection data (e.g., Kleinberg, 1996; Coates et al., 1999).

Synthetic NMR responses of the fully and partially saturated pore size distributions shown in Fig. 14 were generated using Eq. (15) for equally sized circular, equilateral ($\gamma_{1,2,3} = 60^\circ$), and right-angled triangular ($\gamma_1 = 30^\circ, \gamma_2 = 2\gamma_1, \gamma_3 = 3\gamma_1$) pore capillaries (Fig. 13, top left). Two different types of displacement, water drainage and imbibition, in two-phase flow (i.e., water and air), were investigated by simulating water retention curves (Fig. 13) and NMR relaxation signals (Fig. 14). The presented water retention curves for drainage and imbibition were determined from the water distribution inside pores at stationary states.

As expected, water retention curves calculated using the cylindrical model exhibit no hysteresis behavior. In contrast, significant hysteresis between drainage and imbibition





HESSD
11, 12697–12729, 2014



can be observed when using the two triangular capillary models. Note that the calculated water retention curves of the triangular capillary distributions generally exhibit higher saturation levels compared to results for the circular capillaries (∘ symbols in Fig. 13). This is a consequence of pressure-dependent residual water trapped in the pore corners during drainage and imbibition. For the right-angled triangle, the angle becomes more acute, and more water is trapped, which results in the highest saturation levels (◇ symbols in Fig. 13).

Figure 14, left, shows NMR relaxation signals calculated for 20 saturation levels of the simulated drainage and imbibition curves (see Fig. 13) ranging from $S = 100\,\%$ to $S < 1\,\%$ water saturation. Corresponding NMR relaxation time distributions (Fig. 14, right) of the generated NMR transients were determined by means of a regularized multi-exponential fitting using a nonlinear least squares formulation solved by the Levenberg–Marquardt approach (e.g., Marquardt, 1963; Mohnke, 2010). Inverse modeling results of NMR data calculated for the drainage branches using the cylindrical capillary bundle (Fig. 14a) exhibit a shift of the distribution's maximum towards shorter relaxation times with decreasing saturation (i.e., increasing pressure). As anticipated, the derived distribution functions, however, always remain inside the envelope of the relaxation-time distribution curve at full saturation (see also Fig. 1a). In contrast, inversion results for both equilateral (Fig. 14b) and right-angled triangular (Fig. 14c) capillary ensembles show a similar peak-shift to shorter relaxation times but also move outside the initial distribution at full saturation due to NMR signals originating from trapped water in the pore corners of the already de-saturated pore capillaries. In this regard, the peak shift is less prominent for the right-angled triangle capillaries as most of the trapped water in a pore is situated in the acute angle meniscus, i.e. $\gamma_1 = 30^\circ$, which also exhibits longer relaxation times compared to $\gamma_{2,3} = 60^\circ, 90^\circ$ (see Fig. 9). In conclusion, the calculated inverse model based on a triangular capillary bundle qualitatively agrees with the behavior of the NMR relaxation-time distribution at partial saturation observed in experimental data, i.e., of the Rotliegend sandstone shown in Fig. 2.





HESSD
11, 12697–12729, 2014



## 3 Summary and conclusions

Experimental NMR relaxometry data and corresponding relaxation-time distributions obtained at partial water/air saturation were explicated by a modification of conventional NMR pore models using triangular cross-sections. An analytical solution for calculating surface-dominated (fast diffusion) NMR relaxation signals in fully and partially saturated arbitrary angular capillaries, while taking into account residual water trapped in pore corners, was introduced and validated by numerical simulations. In this regard, non-equilateral triangular capillaries at partial saturation exhibit a three-exponential relaxation behavior due to different perimeter-to-surface (= surface-to-volume) ratios of the saturated pore corners.

Furthermore, the shape and size of the triangular pores strongly influence both NMR and hydraulic properties. The NMR relaxation time depends on the surface-to-volume ratio (not on pore shape), while the water distribution inside the pore system, at partial saturation, is strongly influenced by the shape of the pore. Thus, the NMR signal at partial saturation is affected by not only the surface-to-volume ratio, but by the pore shape as well.

Applying the triangular pore models to jointly simulate water retention curves and corresponding NMR relaxometry data for drainage and imbibition allows one to account for hysteresis behavior. The shift of the simulated NMR relaxation distribution functions towards shorter relaxation times below the initial distribution envelope at full saturation is principally in agreement with relaxation behavior observed in experimental NMR data from sandstone reservoir rocks. Ongoing research will include implementation of the introduced approach in an inverse modeling algorithm for NMR data obtained on partially saturated rocks to predict absolute and relative permeability at laboratory and borehole scales. For this purpose, the model will be further developed to also account for adsorbed fluid films and arising contact angle hysteresis during drainage and imbibition.





HESSD
11, 12697–12729, 2014



*Acknowledgements.* The study was supported by the German Research Foundation (DFG) in the framework of the Transregional Collaborative Research Centre 32 (SFB TR 32) and Wintershall AG in the framework of Wintershall Tight Gas Consortium at RWTH Aachen University.

## References

Al-Mahrooqi, S. H., Grattoni, C. A., Muggeridge, A. H., Zimmermann, R. W., and Jing, X. D.: Pore-scale modelling of NMR relaxation for the characterization of wettability, J. Petrol. Sci. Eng., 52, 172–186, 2006.

Applied Reservoir Technology Ltd.: The NMR Sandstone Rock Catalogue, Long Melford, Suffolk, UK, 1996.

Arnold, J., Clauser, C., Pechnig, R., Anferova, S., Anferov, V., and Blümich, B.: Porosity and permeability from mobile NMR core-scanning, Petrophysics, 47, 306–314, 2006.

Blunt, M. J., Jackson, M. D., Piri, M., and Valvatne, P. H., Detailed physics, predictive capabilities and macroscopic consequences for pore-network models of multiphase flow, Adv. Water Resour., 25, 1069–1089, 2002.

Brownstein, K. and Tarr, C. C.: Importance of classical diffusion in NMR studies of water in biological cells, Phys. Rev. A, 19, 2446–2453, 1979.

Chen, S., Liaw, H. K., and Watson, A. T.: Measurements and analysis of fluid saturation-dependent NMR relaxation and linebroadening in porous media, Magn. Reson. Imaging, 12, 201–202, 1994.

Coates, G. R., Xiao, L., and, Prammer, M. G.: NMR Logging Principles and Applications, Halliburton Energy Services, Houston, TX, 234 pp., 1999.

Costabel, S. and Yaramanci, U.: Relative hydraulic conductivity in the vadose zone from magnetic resonance sounding – Brooks–Corey parameterization of the capillary fringe, Geophysics, 76, G61–G71, doi:10.1190/1.3552688, 2011.

Costabel, S. and Yaramanci, U.: Estimation of water retention parameters from nuclear magnetic resonance relaxation time distributions, Water Resour. Res., 49, 2068–2079, doi:10.1002/wrcr.20207, 2013.





HESSD

11, 12697–12729, 2014



Desbois, G., Urai, J. L., Kukla, P. A., Konstanty, J., and Baerle, C.: High-resolution 3-D fabric and porosity model in a tight gas sandstone reservoir: a new approach to investigate microstructures from mm- to nm-scale combining argon beam cross-sectioning and SEM imaging, J. Petrol. Sci. Eng., 78, 243–257, doi:10.1016/j.petrol.2011.06.004, 2011.

Dong, M. and Chatzis, I.: The imbibition and flow of a wetting liquid along the corners of a square capillary tube, J. Colloid Interf. Sci., 172, 278–288, 1995.

Dunn, K. J., Bergman, D. J., and LaTorraca, G. A.: Nuclear Magnetic Resonance: Petrophysical and Logging Applications, Pergamon, Elsevier Science, Amsterdam, 2002.

Finjord, J., Hiorth, A., a Lad, U. H., and Skjaeveland, S. M.: NMR for equilateral triangular geometry under conditions of surface relaxivity – analytical and random walk solution, Transport Porous Med., 69, 33–53, arXiv:cond-mat/0508412v2, 2006.

Fleury, M., Deflandre, F., and Godefroy, S.: Validity of permeability prediction from NMR measurements, CR Acad. Sci. Series II C, 4, 869–872, doi:10.1016/S1387-1609(01)01343-3, 2001.

Ioannidis, M., Chatzis, I., Lemaire, C., and Perunarkilli, R.: Unsaturated hydraulic conductivity from nuclear magnetic resonance measurements, Water Resour. Res., 42, W07201, doi:10.1029/2006WR004955, 2006.

Jia, P., Dong, M., and Dai, L.: Threshold pressure in arbitrary triangular tubes using RSG concept for all wetting conditions, Colloid. Surface A, 302, 88–95, 2007.

Kenyon, W.: Petrophysical principles of applications of NMR logging, Log. Anal., 38, 21–43, 1997.

Kleinberg, R. L.: Utility of NMR T2 distributions, connection with capillary pressure, clay effect, and determination of the surface relaxivity parameter $\rho 2$, Magn. Reson. Imaging, 14, 761–767, doi:10.1016/S0730-725X(96)00161-0, 1996.

Lenormand, R., Zarcone, C., and Sarr, A.: A mechanisms of the displacement of one fluid by another in a network of capillary ducts, J. Fluid Mech., 135, 337–353, 1983.

Liaw, H.-K., Kulkarni, R., Chen, S., and Watson, A. T.: Characterization of fluid distributions in porous media by NMR techniques, AICHE J., 42, 538–546, doi:10.1002/aic.690420223, 1996.

Marquardt, D. W.: An algorithm for the least-squares estimation of nonlinear parametersapll, Siam J. Appl. Math., 11, 431–441, 1963.

Mason, G. and Morrow, N. R.: Capillary behavior of a perfectly wetting liquid in irregular triangular tubes, J. Colloid Interf. Sci., 141, 262–274, 1991.





HESSD
11, 12697–12729, 2014



Mayer, R. P. and Stowe, R. A.: Mercury porosimetry-breakthrough pressure for penetration between packed spheres, J. Colloid Interf. Sci., 20, 893–911, 1965.
Mohnke, O.: Improved forward and inverse modelling of Surface NMR relaxation signals using multi-exponential decomposition, Ph.D. thesis, Technical University Berlin, Berlin, 2010.
Mohnke, O. and Klitzsch, N.: Microscale simulations of nmr relaxation in porous media considering internal field gradients, Vadose Zone J., 9, 846–857, doi:10.2136/vzj2009.0161, 2010.
Or, D. and Tuller, M.: Flow in unsaturated fractured porous media: hydraulic conductivity of rough surfaces, Water Resour. Res., 36, 1165–1177, doi:10.1029/2000WR900020, 2000.
Princen, H. M.: Capillary phenomena in assemblies of parallel cylinders, I. Capillary rise between 2 cylinders, J. Colloid Interf. Sci., 30, 69–75, 1969a.
Princen, H. M.: Capillary phenomena in assemblies of parallel cylinders, II. Capillary rise in systems with more than 2 cylinders, J. Colloid Interf. Sci., 30, 359–371, 1969b.
Princen, H. M.: Capillary phenomena in assemblies of parallel cylinders, III. Liquid columns between horizontal parallel cylinders, J. Colloid Interf. Sci., 34, 171–184, 1970.
Ransohoff, T. C. and Radke, C. J.: Laminar flow of a wetting liquid along the corners of a predominantly gas-occupied noncircular pore, J. Colloid Interf. Sci., 121, 392–401, 1987.
Seevers, D. O.: A Nuclear Magnetic Method for Determining the Permeability of Sandstones, Society of Professional Well Log Analysts, Vol. 6, paper L, Housten, Texas, 1966.
Stingaciu, L. R.: Characterization of natural porous media by NMR and MRI techniques: high and low magnetic field studies for estimation of hydraulic properties, Ph.D. thesis, RWTH Aachen, available at: http://darwin.bth.rwth-aachen.de/opus3/volltexte/2010/3392/ (last access: 30 June 2014), 2010.
Stingaciu, L. R., Weihermüller, L., Haber-Pohlmeier, S., Stapf, S., Vereecken, H., and Pohlmeier, A.: Determination of pore size distribution and hydraulic properties using nuclear magnetic resonance relaxometry: a comparative study of laboratory methods, Water Resour. Res., 46, 1–11, doi:10.1029/2009WR008686, 2010.
Talabi, O., AlSayari, S. Iglauer, I., and Blunt, J.: Pore-scale simulation of NMR response, J. Petrol. Sci. Eng., 67, 168–178, 2009.
Tokunaga, T. K. and Wan, J.: Water film flow along fracture surfaces of porous rock, Water Resour. Res., 33, 1287–1295, doi:10.1029/97WR00473, 1997.
Toledo, P. G., Novy, R. A., Davis, H. T., and Scriven, L. E.: Hydraulic Conductivity of Porous Media at Low Water Content, Soil Sci. Soc. Am. J., 54, 673–679, doi:10.2136/sssaj1990.03615995005400030007x, 1990.





HESSD
11, 12697–12729, 2014



Torrey, H. C.: Bloch equations with diffusion terms, Phys. Rev., 104, 563–565, doi:10.1103/PhysRev.104.563, 1956.

Tuller, M. and Or, D.: Hydraulic conductivity of variably saturated porous media: film and corner flow in angular pore space, Water Resour. Res., 37, 1257–1276, doi:10.1029/2000WR900328, 2001.

Tuller, M., Or, D., and Dudley, L. M.: Adsorption and capillary condensation in porous media – liquid retention and interfacial configurations in angular pores, Water Resour. Res., 35, 1949–1964, doi:10.1029/1999WR900098, 1999.





HESSD

11, 12697–12729, 2014



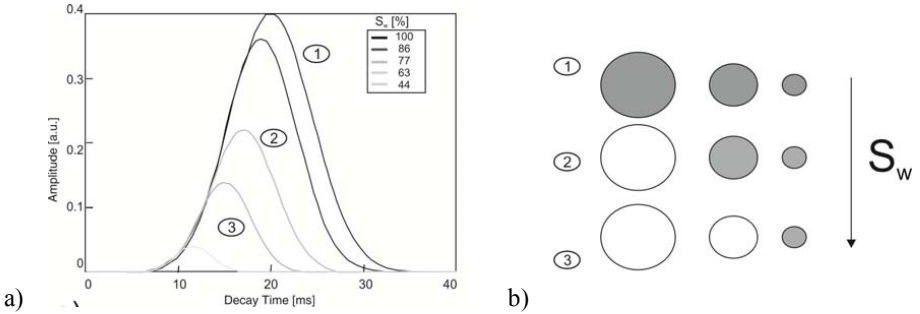


**Figure 1. (a)** NMR decay time distributions at different water saturation levels for a classical cylindrical capillary pore distribution. **(b)** Concept sketch of saturated (gray) and de-saturated capillaries, e.g., during drainage.





HESSD
11, 12697–12729, 2014



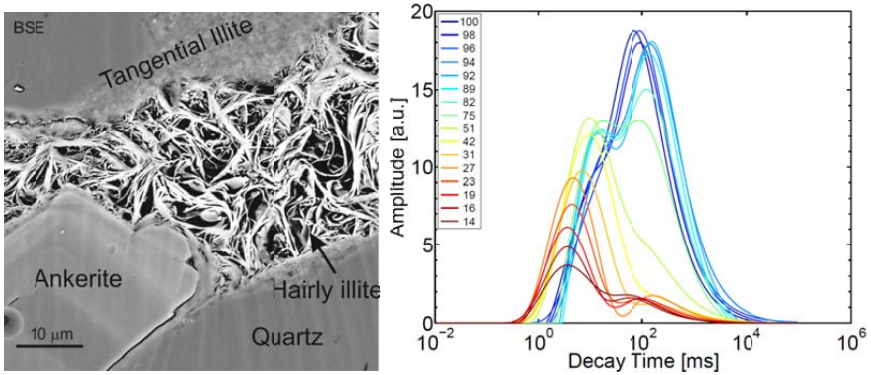


a) b)

**Figure 2. (a)** Complex pore structure of a Rotliegend tight gas sandstone. Pore spaces are filled with tangential and hairly illite and exhibit different pore types with elongated or slit-shaped, triangular, and multi-angular cross-sections. **(b)** $T_1$ decay time distributions calculated from inverse Laplace transform performed on Rotliegend sandstone (porosity 13 %, permeability 0.1 mD) at different water saturations ($S_w$ = 14–100 %).





HESSD
11, 12697–12729, 2014



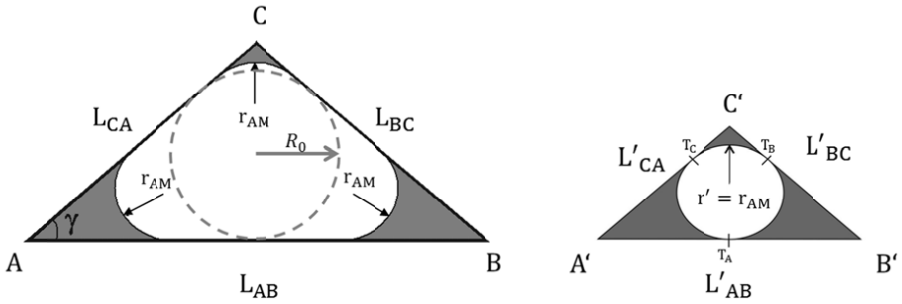


**Figure 3.** Cross-sections of a partially saturated triangular tube. Arc meniscus of radius $r_{AM}$ separates invading non-wetting phase (white) from adsorbed wetting phase (gray). **(a)** Original triangle $ABC$ with side lengths $L_{AB}$, $L_{BC}$, $L_{CA}$, and radius $R_0$ of its inscribing circle. **(b)** Reduced triangle $A'B'C'$ of similar geometry. The wetting phase resides in the three corners (gray) with $r' = r_{AM}$ being the radius of both the three interface arc menisci of $ABC$ and of the inscribing circle of $A'B'C'$.





HESSD
11, 12697–12729, 2014



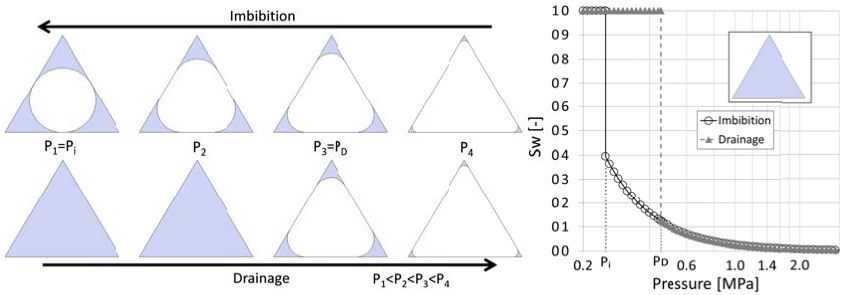


a) b)

**Figure 4. (a)** Modeled distribution of water (gray) and gas (white) phases in an equilateral triangular tube with a side length of 1 µm during imbibition (top) and drainage (bottom). **(b)** Water saturation vs. capillary pressure during imbibition (∘) and drainage (▲).





HESSD
11, 12697–12729, 2014



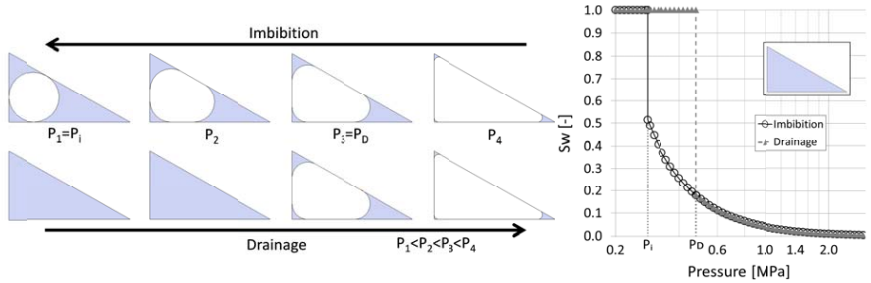


a) b)

**Figure 5. (a)** Modeled distribution of water (gray) and gas (white) phases in a right-angled triangular capillary ($G = 0.39$) with side lengths $L = 1, 0.81, 0.58\,\mu m$, and perimeter $P = 2.39\,\mu m$ during imbibition (top) and drainage (bottom). **(b)** Water saturation vs. capillary pressure during imbibition (∘) and drainage (▲).





HESSD
11, 12697–12729, 2014



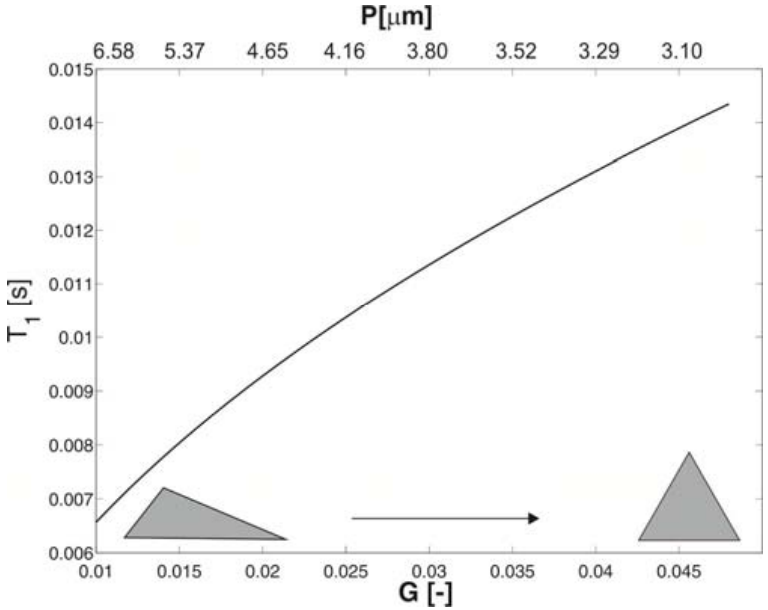


**Figure 6.** Longitudinal relaxation times $T_1$ of fully saturated triangular pores with constant cross-sectional area $A = 4.33 \times 10^{-13}\,\mathrm{m}^2$ vs. shape factor $G = \frac{A}{P^2}$ and perimeter $P$. NMR parameters: $\rho_s = 10\,\mu\mathrm{m\,s}^{-1}, T_{1B} = 3\,\mathrm{s}$.





HESSD
11, 12697–12729, 2014



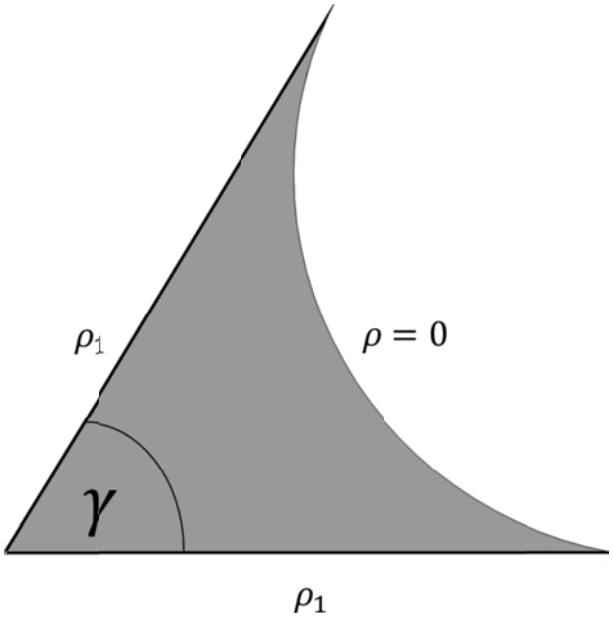


**Figure 7.** Saturated corner with active boundaries, i.e., $\rho = \rho_1 > 0$ at the corner's perimeter $P_\gamma$ and a passive boundary at the air–water interface (meniscus), i.e., $\rho = 0$.





HESSD
11, 12697–12729, 2014



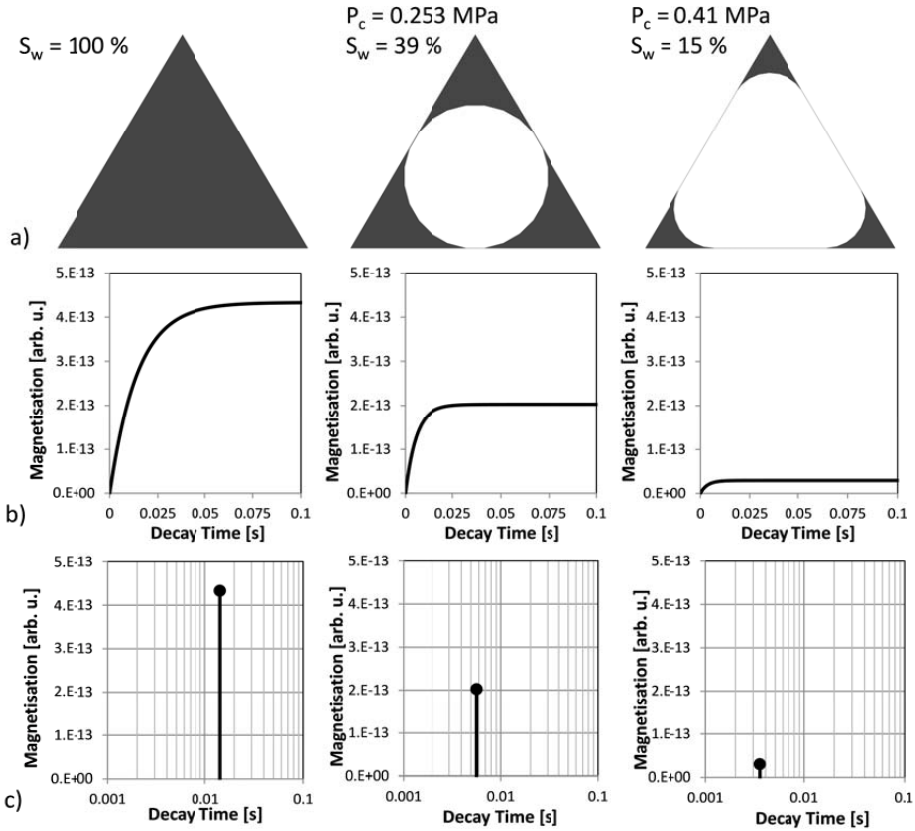


**Figure 8.** Water (black) and air (white) distributions within a triangular pore ($A_0 = 4.33 \times 10^{-13}\,m^2, \rho_s = 10^{-5}\,m$) at different capillary pressures for imbibition **(a)** with corresponding evolution of magnetization **(b)** and NMR $T_1$ relaxation times **(c)**.





HESSD
11, 12697–12729, 2014



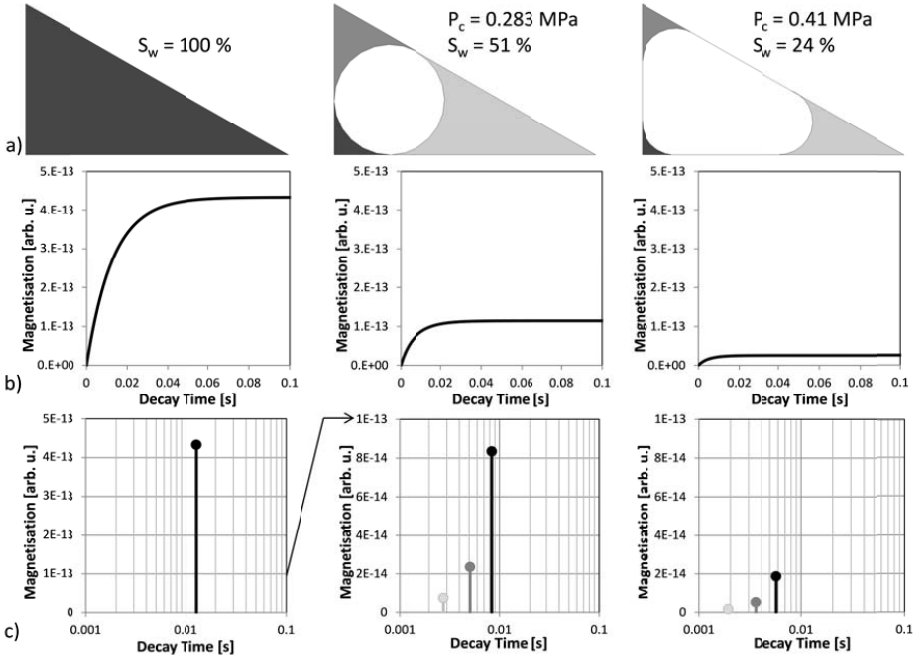


**Figure 9.** Water (black and grays) and air (white) distributions within a right-angled triangular pore ($A_0 = 4.33 \times 10^{-13}\,\mathrm{m}^2, \rho_s = 10^{-5}\,\mathrm{m\,s}^{-1}$) at different capillary pressures for imbibition **(a)** with corresponding evolution of magnetization **(b)** and NMR $T_1$ relaxation times **(c)**.





HESSD
11, 12697–12729, 2014



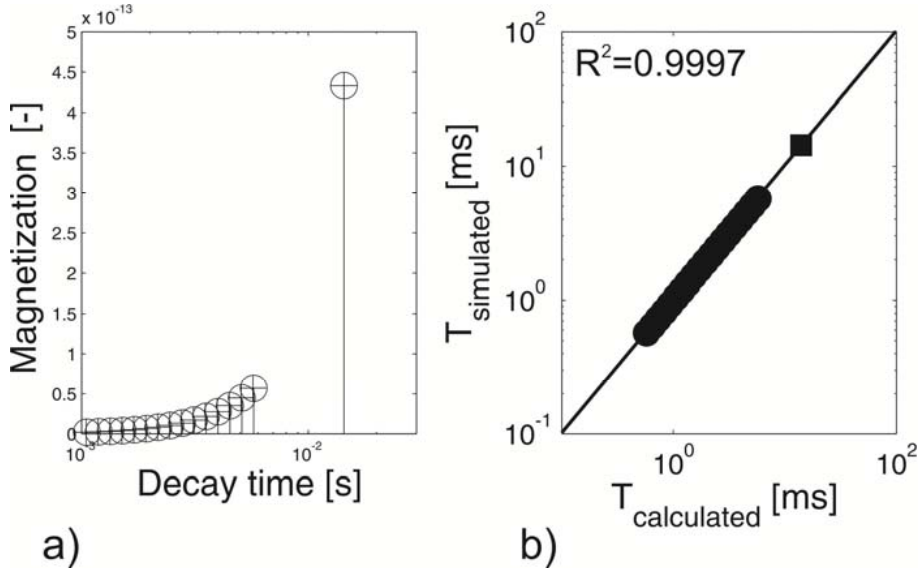


**Figure 10.** NMR response of an equilateral triangular capillary pore model (with a side length of 1 µm). **(a)** $T_1$ decay time data of numerical (∘) and analytical solutions (+) for all applied pressure levels. **(b)** Cross-plot of numerically simulated and analytically calculated relaxation times at partial (•) and full water saturation (■). A corresponding water saturation vs. capillary pressure diagram is shown in Fig. 4.





HESSD
11, 12697–12729, 2014



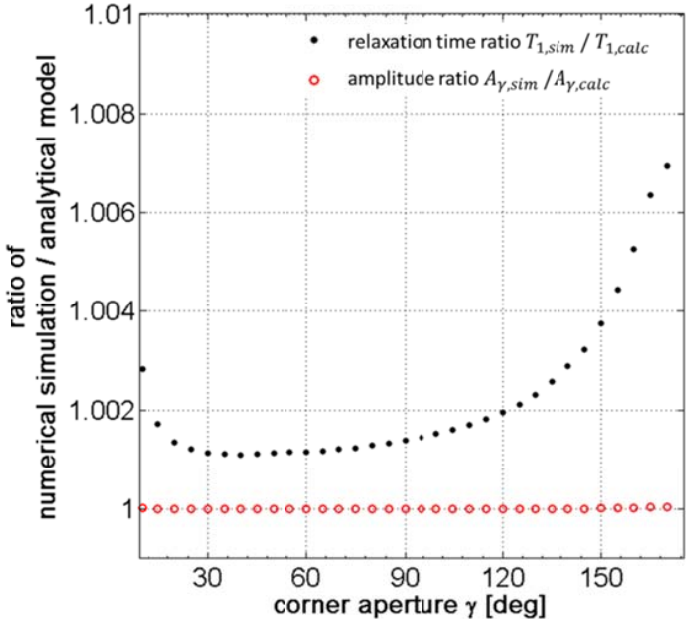


**Figure 11.** Comparison of analytical and calculated NMR relaxometry data originating from saturated pore corners (e.g. see Fig. 7) of varying apertures ($5^\circ < \gamma < 175^\circ$) and equal active surface-to-volume ratio $\frac{P_{\gamma_i}}{A_{\gamma_i}}$ = const. (NMR model parameters; $T_{1B} = 3\,\mathrm{s}$, $D = 2.5 \times 10^{-9}\,\mathrm{m^2\,s^{-1}}$, $\rho_s = 10\,\mu\mathrm{m\,s^{-1}}$).





HESSD
11, 12697–12729, 2014



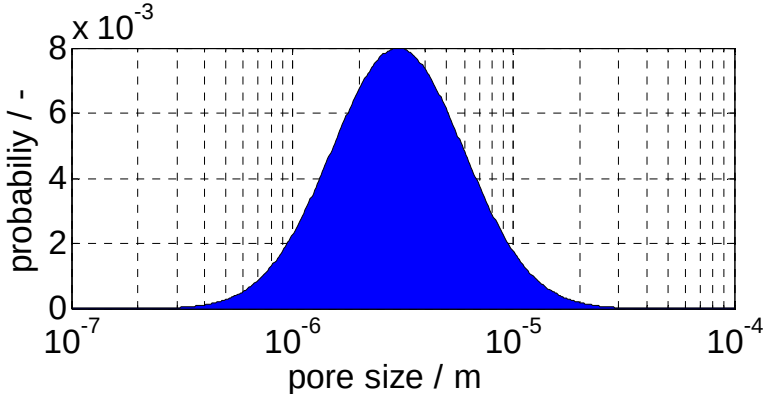


**Figure 12.** Pore-size distribution model in analogy to that of the Rotliegend Sandstone shown in Fig. 2.





HESSD
11, 12697–12729, 2014



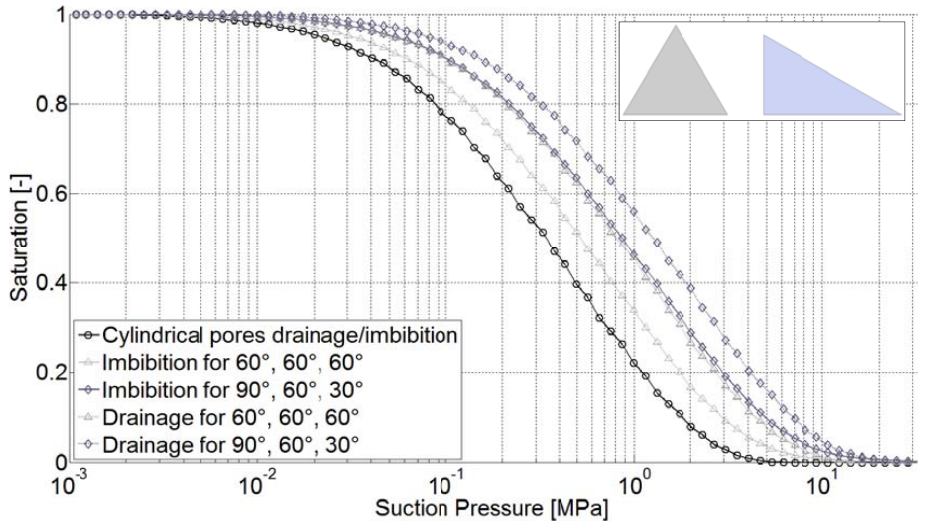


**Figure 13.** Drainage (dotted lines) and imbibition (solid lines) curves for three different pore distributions with circular (black circles), equilateral (gray triangles), and right-angled (90°, 60°, 30°; diamonds) cross-sections. Note that at a certain pressure the circular cross-section shows the highest desaturations levels, followed by the equilateral triangle. The right-angled triangle has the highest saturation due to water trapped in the smaller angle.





HESSD
11, 12697–12729, 2014



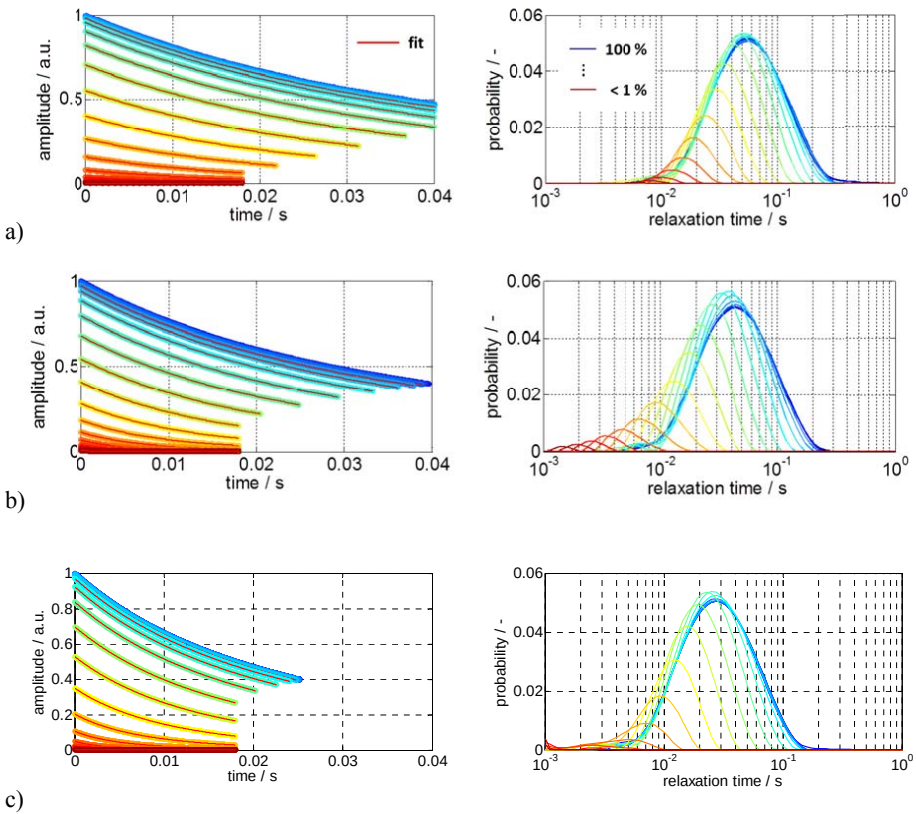


**Figure 14.** Calculated and fitted (red lines) NMR transient signals (left) for one fully and 19 partially saturated pore-size distributions using circular **(a)**, equilateral **(b)**, and right-angled **(c)** capillaries and corresponding inverted NMR relaxation time distributions (right).





HESSD
11, 12697–12729, 2014